Article

Radar evidence of an accessible cave conduit on the Moon below the Mare Tranquillitatis pit

Leonardo Carrer ⓘ [1] ✉, Riccardo Pozzobon ⓘ [2,3,4,5], Francesco Sauro ⓘ [5], Davide Castelletti[6], Gerald Wesley Patterson[7] & Lorenzo Bruzzone ⓘ [1]✉

Several potential subsurface openings have been observed on the surface of the Moon. These lunar pits are interesting in terms of science and for potential future habitation. However, it remains uncertain whether such pits provide access to cave conduits with extensive underground volumes. Here we analyse radar images of the Mare Tranquillitatis pit (MTP), an elliptical skylight with vertical or overhanging walls and a sloping pit floor that seems to extend further underground. The images were obtained by the Mini-RF instrument onboard the Lunar Reconnaissance Orbiter in 2010. We find that a portion of the radar reflections originating from the MTP can be attributed to a subsurface cave conduit tens of metres long, suggesting that the MTP leads to an accessible cave conduit beneath the Moon's surface. This discovery suggests that the MTP is a promising site for a lunar base, as it offers shelter from the harsh surface environment and could support long-term human exploration of the Moon.

The presence of conduits below the lunar surface has been theorized and extensively debated for at least 50 yr (refs. [1–3]). The first evidence of collapse pits that potentially provide access to cave conduits emerged from an analysis of data acquired by the Selenological and Engineering Explorer (SELENE)[4] in 2009, which has subsequently been confirmed by images captured by the Lunar Reconnaissance Orbiter's camera (LROC) since 2012[5]. Although more than 200 pits have now been detected in various lunar geological settings and latitudes[6], it remains uncertain whether any of these openings could lead to extended cave conduits underground. Attempts have been made to identify cave conduits near the pits using nadir-looking orbital ground-penetrating radar[7,8], gravimeters[9] and radiometers[10]. However, the results of these experiments are inconclusive[11]. For some pits in the lunar maria, the presence of overhangs, discernible as shadowed areas in optical images, suggests the existence of underlying conduits or at least larger void spaces[5]. Nevertheless, a direct observation and quantitative estimate of their extension beyond the visible pit floor is still lacking. The exploration of lunar caves through future robotic missions could provide a fresh perspective on the lunar subsurface and yield new insights into the evolution of lunar volcanism[12]. Furthermore, direct exploration could confirm the presence of stable subsurface environments shielded from radiation[13] and with optimal temperature conditions for future human utilization[10]. However, such robotic missions would face important challenges in navigating unknown terrains without available predictions regarding the extension and morphology of such conduits. Therefore, to initiate the exploration of lunar cave conduits, it is of utmost importance to gather evidence to determine which lunar pits can offer access to extended cave conduits.

Recent works in the literature have demonstrated that side-looking orbital synthetic aperture radar (SAR) imaging systems, operating in the gigahertz frequency range, can detect cave conduits and determine their characteristics and accessibility in terrestrial environments

[1]University of Trento, Trento, Italy. [2]Department of Geosciences, University of Padova, Padua, Italy. [3]Department of Physics and Astronomy, University of Padova, Padua, Italy. [4]Centro di Ateneo di Studi ed Attività Spaziali 'G. Colombo', University of Padova, Padua, Italy. [5]La Venta Geographic Exploration APS, Treviso, Italy. [6]Capella Space Corporation, San Francisco, CA, USA. [7]Johns Hopkins University Applied Physics Laboratory, Laurel, MD, USA. ✉e-mail: leonardo27@gmail.com; lorenzo.bruzzone@unitn.it
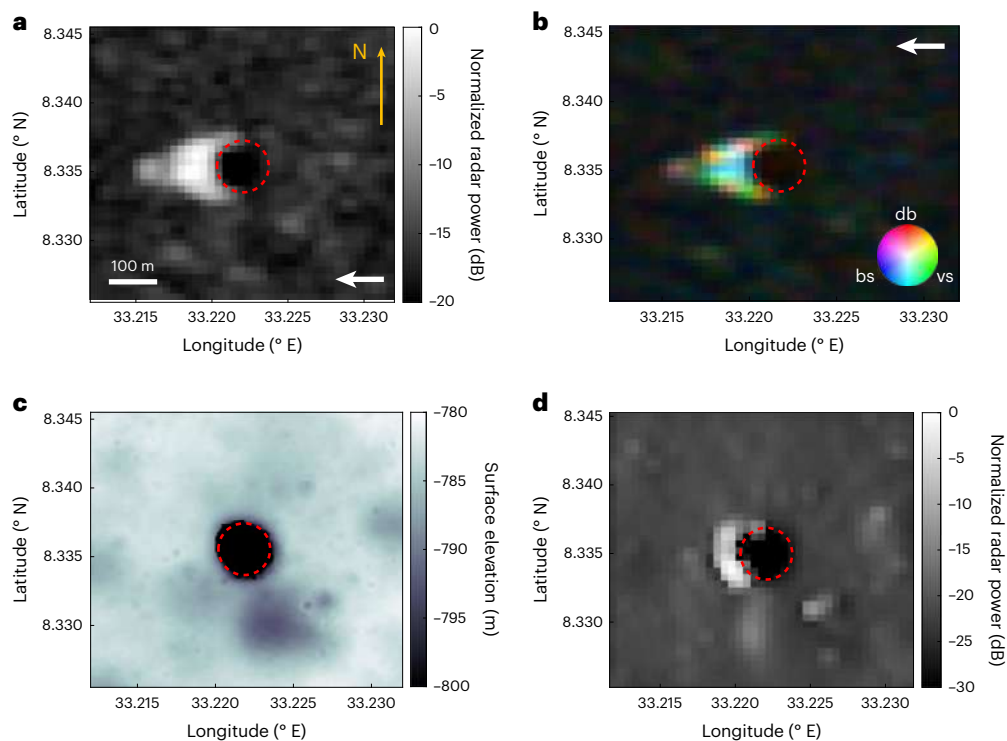
Fig. 1 | Experimental results for the MTP (8.3355° N, 33.222° E) imaging with Mini-RF. a,b, Mini-RF SAR image of the MTP (lsz_06587_2s1_eku_10n033) (**a**) and its corresponding RGB m-chi polarimetric decomposition (red, double bounce; blue, single scattering; green, volume scattering) (**b**). The MTP overhang and cave conduit radar echoes exhibit single- and double-bounce scattering, respectively.

This is compatible with the radar model of backscattering from subsurface conduits[14]. **c**, DTM from stereo observations (NAC_DTM_TRANQPIT1)[23] limited to the pit walls visible in LRO NAC images. **d**, 3D radar simulation of the DTM in **c**. The red dashed circle delineates the edge of the pit. The radar look direction is indicated with a white arrow.

in the proximity of collapse pits[14]. Under the right conditions, the side-looking acquisition geometry enables the radiated electromagnetic field to penetrate the pit and partially illuminate the shadowed subterranean conduit to generate measurable radar echo signals. Consequently, this type of system holds relevant potential for the remote detection and characterization of planetary conduits. One such system is the miniature radio-frequency instrument (Mini-RF), a polarimetric synthetic aperture imaging radar orbiting the Moon onboard the Lunar Reconnaissance Orbiter (LRO)[15,16]. From 2009 to 2011, Mini-RF captured lunar surface images at a maximum resolution of approximately 15 m (azimuthal) × 30 m (range) until its transmitter experienced a critical failure. Although currently only occasionally operated in bistatic mode, Mini-RF has obtained several images of lunar pits, including the Mare Tranquillitatis pit (MTP) in monostatic mode.

The Mini-RF dataset provides an opportunity to assess whether the recorded radar reflections from the MTP indicate the presence of an accessible subsurface cave conduit and to determine the three-dimensional (3D) geometric attributes of the conduit. Additionally, it allows for the verification of hypotheses concerning the genesis of both the MTP itself and the cave conduit.

Characteristics of the MTP

First detected in 2009[4], the MTP has since been characterized with photogrammetric measurements as the deepest known pit on the Moon[17]. It opens as a cylindrical hole reaching $D = 100$ m in diameter (measured in the east–west direction) in the basaltic flows of Mare Tranquillitatis[18] (8.3355° N, 33.2220° E). A table with all MTP morphometric data, LROC datasets and geological features is available in the Lunar Pit Atlas from the LROC team[19]. Due to its peculiar morphology, it is considered to be a potential opening on a cave roof. Some authors have referred to it as a subsurface access point[20,21] or a special pit candidate[22]. The MTP is not associated with other pits (the closest known is the south-west Mare

Tranquillitatis pit 290 km away), and no rilles or other volcanic or tectonic geomorphological features are visible on the surface. Hypotheses for its formation include a roof collapse over a lava tube, ceiling stoping of a near-surface intrusive magmatic structure, or a collapse feature above a tectonically produced void[17]. Recent stereo analysis using image pairs taken by the narrow angle camera (NAC) onboard the LRO allowed a partial 3D reconstruction[17] of the pit walls and floor (Extended Data Fig. 1; see Methods for descriptions of all the variables displayed in the figure). Below a sloping funnel of depth 15–30 m with respect to the surrounding surface, the pit walls become vertical (approximately ±15°) down to a depth denoted as $H = 75$–80 m, where the east side overhangs 20–40°. The west side overhangs at the same depth but with a more regular inclination of 10°. From optical observation, the void appears to extend both to the west and the east following the overhang morphology. The floor of the pit is covered by boulders up to 10 m in diameter embedded in more fine-grained material. The floor slopes down between 10° and 20° to a visible depth of 125 m on the west side and 135 m on the eastern one. The deepest point of the stereo model is below the north-west rim. These morphometric parameters cover almost all the potential view area of an orbiting optical camera. There is no possibility of looking further into the subsurface, mainly because of geometric and solar illumination constraints.

Detection of a cave conduit from analysing Mini-RF data

In the considered Mini-RF acquisition of the MTP, the radar antenna illuminated the MTP from east to west with a look angle θ_L of 48.9° (Extended Data Fig. 1). The Mini-RF orbit track and radar antenna were oriented in the north–south direction (the radar azimuth axis) and the east–west direction (the radar range axis), respectively. The angle between the radar range axis and the MTP diameter was 0.22°. Accordingly, the acquisition was about parallel to the MTP diameter measured
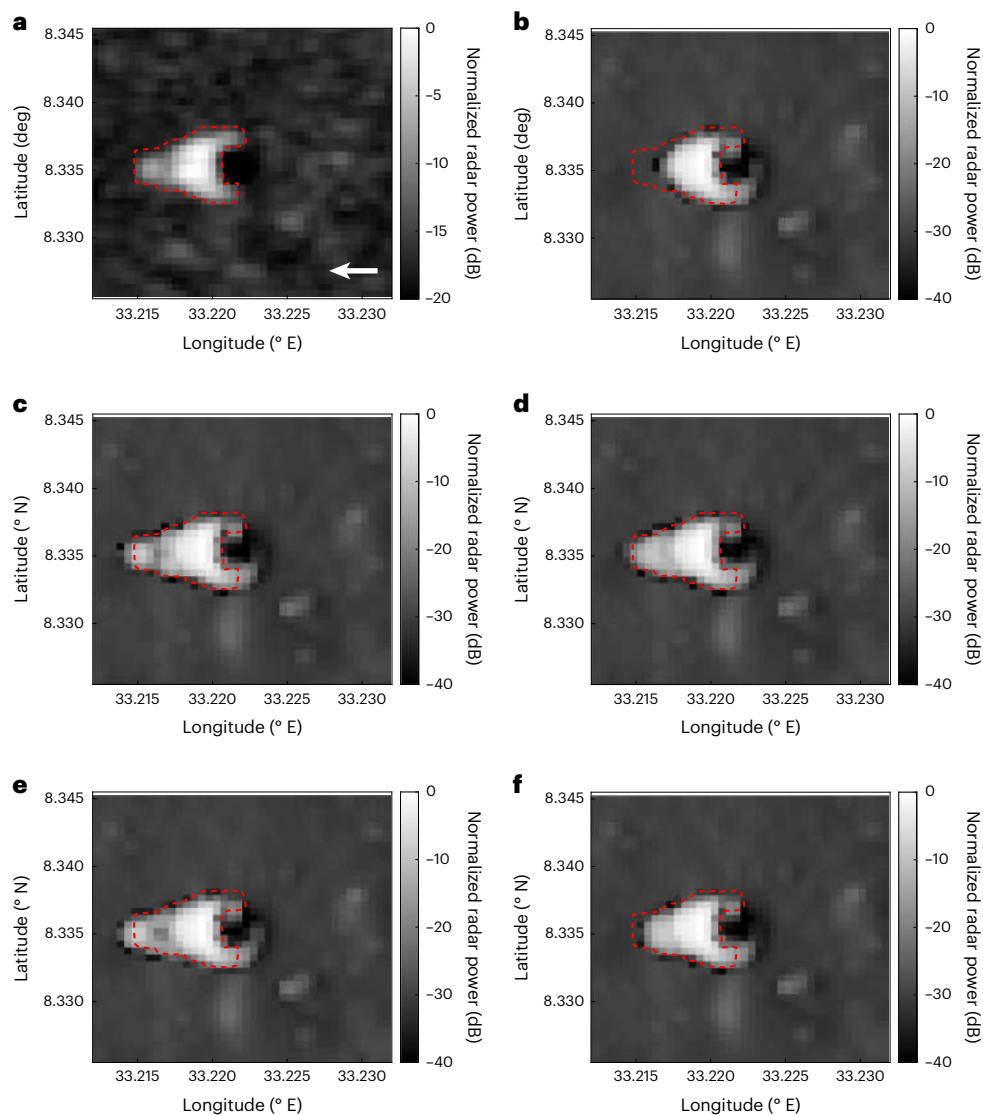
Fig. 2 | Results for MTP radar simulations (8.3355° N, 33.222° E). a, Mini-RF SAR image of the MTP (lsz_06587_2s1_eku_10n033). **b**, 3D radar simulation[24] of Wagner and Robinson's[17] 3D pit model (surface and overhang). **c,d**, 3D radar simulation of model A (**c**; Fig. 3a) and model B (**d**; Fig. 3b). **e**, 3D radar simulation of a model with a cave conduit having a roof and floor slope of 5°. **f**, 3D radar simulation of a model with a cave conduit having a roof and floor slope of 70°. The red dashed lines mark the outline of the anomaly in the experimental data in **a**. The comparison of experimental and simulated data implies that an accessible conduit-like cave is present below the MTP west wall.

in the east–west direction. The incident radar radiation could propagate below the western pit wall[14] if $\theta_L \leq \tan^{-1}(D/H)$, where H is the pit wall height. For the MTP, this results in $\theta_L \leq 51.34°$. This requirement is met in the considered acquisition.

Figure 1a shows a Mini-RF radar image (total backscattered power) of the MTP. The image reveals an anomalous increase in radar echo power originating beyond the west side of the pit. To rule out that the bright reflections originated from the surface, we used a mesh, generated by a Poisson surface reconstruction, of the digital terrain model (DTM) from LRO NAC[23] (Fig. 1c) to simulate the radar reflections due to the surface morphology only (Fig. 1d). The resolution of the DTM is 2 m per pixel. The comparison clearly shows that the anomalous reflection did not originate from the surface. Instead, the morphology and characteristics of these anomalous reflections are strikingly similar with what has been observed on several terrestrial cave analogue sites with a comparable orbital radar sensor[14] (Extended Data Fig. 2). In the terrestrial case, the anomalous reflections were attributed to the radar response of the skylight overhang and subsurface conduit by comparison with 3D radar simulations of the ground truth[14]. The analysis of the

m-chi polarimetric decomposition of the radar image (Fig. 1b) reveals that the reflections from the hypothesized MTP subsurface conduit are compatible with single- and double-bounce scattering. This is in line with the expected scattering mechanism of a subsurface conduit[14].

To confirm that the anomalous increase in brightness can be attributed to subsurface features of the MTP, we performed a series of 3D radar simulations[24] of different potential geometries of the pit and an associated subsurface cave conduit (Fig. 2). First, we performed a simulation taking as input the mesh obtained by a Poisson surface reconstruction of the available 3D model (surface, the pit walls and the overhangs) of the MTP, as reconstructed by Wagner and Robinson[17]. The result of this simulation (Fig. 2b) shows, by comparison with Fig. 2a, that the brighter and wider part of the anomalous radar reflection can be attributed to the overhang reconstructed by Wagner and Robinson[17]. However, the second, weaker and narrower part of the reflection is not justified by this model. Based on the large amount of observation and results obtained for terrestrial analogues, these narrow and rectangular reflections can be attributed to the response of subsurface conduits (Extended Data Fig. 2e).
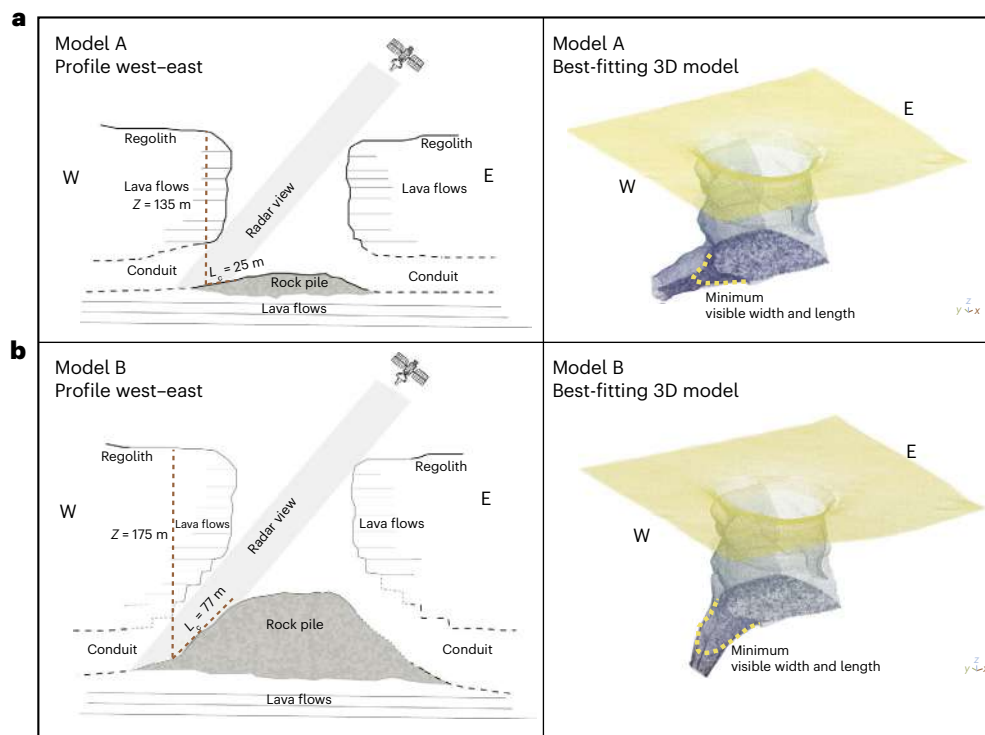
Fig. 3 | Reconstructed MTP cave conduit based on an inversion of the the Mini-RF radar data. a,b, Model A (**a**; Fig. 2c) and model B (**b**; Fig. 2d) side view and 3D model. Models A and B represent the best-fitting scenarios for the Mini-RF radar response from the MTP. Model A is a conduit with a floor slope of about 3° ± 2.5°. Model B is a conduit with a roof slope of about 55° ± 5° and a floor slope of about 45° ± 5°. The surface and overhang are modelled based on Wagner and Robinson's 3D model[17]. The cave conduit, developing from the bottom of the MTP, is modelled based on an inversion of the Mini-RF data. The 3D models on the right of the panels are colour-coded according to the depth of the points below the surface (red, low depth and green/blue, high depth). The solid and dashed lines of the side-view representation depict what is observed and hypothesized of the pit morphology, respectively.

The hypothesis of a lava tube collapse origin for the MTP implies the presence of a cave conduit extending further from the pit walls. The material collapsed from the roof during the opening of the pit should have formed a cone of detritus corresponding to the observable pit floor, which is partially visible in the photogrammetric reconstruction by Wagner and Robinson[17]. The slope of the detrital cone should decrease with distance from the centre of the pit, with an angle of repose due to a mixture of rocks and regolith[17]. There should be an approximately horizontal development at the depth of the horizontal conduit floor. The radar signal should extend further underground to intersect either the floor of the horizontal conduit or the detrital, sloping pit floor, if the cave conduit is deeper than the radar view (Extended Data Fig. 1).

3D radar simulations of the cave conduit model

Given the geologic assumptions about the potential geometric characteristics of the cave conduit, we produced a series of radar response simulations using a set of representative conduit morphologies extended from Wagner and Robinson's overhang model[17], each with different conduit roof and floor slopes (while maintaining the observed conduit geometry in plan view) and taking into account the specific Mini-RF acquisition geometry over the pit (Methods). These simulations also considered the pixel resolution of Mini-RF of 15 m (azimuthal) × 30 m (range) and, thus, the uncertainty on the radar-measured parameters. The simulated 3D radar responses are shown in Fig. 2 and Extended Data Figs. 3 and 4. The end-member geometries fitting the experimental data best (Extended Data Fig. 5) are shown in Fig. 2c,d. These best-fitting models maximize the correlation coefficient between the simulated and experimental radar images (Methods). The first (Fig. 2c) corresponds to geometric model A (Fig. 3), which is a conduit with a floor slope of about 3° ± 2.5°, a maximum depth from the surface for reflection of 135 m and

a conduit extension of about 25 m. The second (Fig. 2d) corresponds to model B, a conduit with a roof slope of 55° ± 5° and a floor slope of about 45° ± 5°. The maximum depth for reflection is 175 m, and the conduit extension is estimated to be 77 m. These best-fitting results confirm that the anomalous reflections originated from a subsurface conduit. The estimated width of the tunnel for both models A and B is similar at 45 ± 7.5 m. However, these radar simulations assumed a parametric value for the conduit width (Extended Data Figs. 6 and 7) and found that Mini-RF is unable to measure conduit widths larger than 55 m (Extended Data Fig. 7). We attribute this to the combined effect of the considered Mini-RF acquisition geometry (look angle of 48.9°) and the conduit geometry, which resulted in only a portion of the lateral extension of the cave being observed (Methods). Accordingly, the conduit lateral extension could be much larger than what is possible to estimate from the considered Mini-RF radar measurements. We also tested alternative hypotheses with a closed magmatic chamber or with a space due to tectonic extension[17], which do not provide access to a cave system (Fig. 2f). Thus, the 3D radar simulations that assume a small void with a steep overhang do not match the experimental data (Extended Data Figs. 3e and 4h,n). It is also unlikely that reflections originating from a steep secondary overhang would result in double-bounce scattering (Fig. 1b), as was observed in the experimental data for the hypothesized conduit.

The simulations show that the experimental observation is compatible only with a conduit-type cave expanding underground from the west side of the pit. In model A, considering the 3° average slope of the pit floor towards the west, the observed radar signal anomaly is limited in extension only because it intersects the floor slope approximately 25 m inside the conduit, which is within the range of floor slopes estimated by optical stereo imagery. In this case, the conduit would be mainly horizontal. Instead, in model B, we observe the floor sloping

down at the side of a much bigger and steeper detrital floor cone, which intersects the floor at a depth of 175 m. This scenario is more compatible with the natural characteristics of a pit that formed due to the collapse of a conduit ceiling, where the detrital cone formed by the fallen material should occupy approximately the same volume and reach similar depths as the pit itself. In this case, the conduit at the bottom of the detrital cone could be much wider than the radar view (Fig. 3).

For model B, an origin due to stoping of the ceiling of a near-surface intrusive magmatic structure (as also observed for terrestrial examples[14]) cannot be completely excluded by the radar observations, but the considerable lateral extension of the void detected by the radar anomaly allows us to identify the lava tube origin of the MTP. Further radar observations from different directions and angles could better resolve the width of the extension of the cave conduit and also the presence of an additional conduit continuation in the opposite direction below the eastern wall.

Discussion and conclusions

Mini-RF was not specifically designed to conduct a survey of the lunar pits. The sensor's resolution of approximately 15 m × 30 m only allows for the evaluation of pits with a diameter greater than about 80 m. The equatorial coverage of the sensor is a fraction of the polar one, resulting in a limited amount of data covering lunar pits. For most of the other lunar pits, only east or west illumination data are available. Given the list of identified lunar pits[6], the constraints imposed by the Mini-RF dataset and the limited sensor resolution, the method did not allow us to identify pits providing a subsurface conduit access other than the MTP. Note that among the pits that can be observed in Mini-RF data, the MTP has the lowest degradation state, as reported by Wagner and Robinson[17]. Thus, it will more probably provide access to a subsurface conduit. Despite the aforementioned limitations, our analysis of a Mini-RF SAR image of the MTP suggests the presence of an important cave void (tens of metres long), which is possibly an elongated conduit, at the bottom of a lunar pit. This observation could indicate that lava tubes or other types of caves are common features below maria regions. This finding is of particular significance as the future direct exploration of such structures could yield vital insights into the emplacement of lunar maria[12] by providing access to samples of superposed lava flows with different ages. This would result in a substantial advancement in the understanding of planetary volcanism[25]. The presented work also implies that SAR imaging is a viable methodology for characterizing and assessing the accessibility of lunar conduits extending from pit entrances[26]. The work presented here could be substantially expanded if radar orbital sensors with a resolution able to resolve the interior of all lunar pits identified by LRO[6] are deployed in lunar orbit. A complete survey of all known lunar pits would allow us to identify the most promising accesses for subsurface lunar exploration and provide information on the potential for installing human lunar base in environments protected from cosmic radiation and with stable temperatures[3]. The same method could also be used on Mars, for which more than 1,000 cave entrances have already been identified[20], to provide unprecedented information on potential astrobiological targets for future missions[27].

Methods

Determining cave parameters from radar data

A cave conduit is characterized by (1) a roof slope θ_R, (2) a floor slope θ_F, (3) a maximum illumination depth z_{ss} and (4) a length L_c (Extended Data Fig. 1). These parameters were determined in the following way. Let us denote the bidimensional coordinates of the reference inner wall, floor and surface points, respectively, as $p_w = (x_w, z_w)$, $p_F = (x_F, z_F)$ and $p_S = (x_s, z_s)$. These points were evaluated with Wagner and Robinson's MTP model[17] (Extended Data Fig. 1). The model is tridimensional. However, the y coordinate (Extended Data Fig. 1) does not play a role in the conduit roof and floor modelling, and thus, it is assumed to be constant and equal to 0 (the pit centre). We first determined the value

of $p_{ss} = (x_{ss}, z_{ss})$, which is the deepest observable conduit subsurface point, given the range $\Delta R_g = \Delta R_m \sin^2(\theta_L) = \Delta R \sin(\theta_L)$ and the look angle θ_L. The variables ΔR_g and ΔR are defined as the ground and slant range intervals, respectively. The value of ΔR_m can be measured directly from an image. It is the length of the image anomaly attributed to the conduit[14]. The Cartesian components of p_{ss} are determined as:

$$x_{ss} = x_w - \Delta R_g. \tag{1}$$

If we assume that $\theta_R < \pi/2 - \theta_L$ and $\theta_F < \pi/2 - \theta_L$, then the radar reflections originate only from the floor. In this case,

$$z_{ss} = \tan \theta_L (x_w - \Delta R_g) + z_w - \tan \theta_L x_w - \varepsilon. \tag{2}$$

If we assume that $\theta_R > \pi/2 - \theta_L$ and $\theta_F > \pi/2 - \theta_L$, then the radar reflections originate only from the roof. In this case,

$$z_{ss} = \tan \theta_L (x_w - \Delta R_g) + z_s - \tan \theta_L x_s + \varepsilon. \tag{3}$$

The variable z_{ss} is interpreted as the maximum conduit depth illuminated by the radar. The variable ε is a margin factor much greater than the radar wavelength λ to prevent the incident radiation rays from colliding with the inner wall point. We assumed that ε is equal to 1 m. When $\theta_R < \pi/2 - \theta_L$ (only floor reflections),

$$\theta_F = \tan^{-1}\left(\frac{z_{ss} - z_F}{x_{ss} - x_F}\right), \tag{4}$$

and the value of θ_R is undefined. When $\theta_R > \pi/2 - \theta_L$ and $\theta_F > \pi/2 - \theta_L$ (reflections from only the roof),

$$\theta_R = \tan^{-1}\left(\frac{z_{ss} - z_w}{x_{ss} - x_w}\right), \tag{5}$$

and the value of θ_F is undefined.

For floor-only reflections, the conduit depth

$$z_c(x) = \tan \theta_c (x - x_{ss}) + z_{ss}, \quad x_{ss} \leq x \leq x_F, \tag{6}$$

and the length of the conduit

$$L_c = \sqrt{(z_{ss} - z_c(x_w))^2 + (x_{ss} - x_w)^2}. \tag{7}$$

For roof-only reflections, L_c is undefined. The equations for the two cases can be combined to give the response in the mixed case ($\theta_R > \pi/2 - \theta_L$ and $\theta_F < \pi/2 - \theta_L$).

The conduit width $w(x)$ is directly inferred from the radar image, as there is no projection involved when measuring the ground range interval of the −3 dB power level of the radar azimuth response attributed to the conduit between the cave walls reflections (along the y direction of Extended Data Fig. 1). The radar-measured conduit width is influenced by several factors, including the acquisition geometry (for example, the look angle θ_L), the conduit inclination (for example, the roof slope θ_R) and the pit diameter. Consequently, the conduit width estimated from radar measurements may be an underestimation of the true value as it depends on the points of intersection between the conduit curvature and the set of oriented electromagnetic waves transmitted from the radar acquisition position. In general, when the conduit width exceeds the pit diameter, only the portion visible within the pit aperture can be measured. The maximum radar-estimated conduit width versus the actual width value has been estimated through simulation, as depicted in Extended Data Fig. 7.

Given the uncertainty on ΔR_m resulting from the Mini-RF pixel resolution, the above equations provide a first estimate of the cave conduit's geometric parameters. The estimates of the geometric

parameters were then further refined by using 3D models and radar simulations.

Generating the 3D models

The initial estimates of the slope, depth and width of the cave conduit, derived from the radar data, were used as input for generating several 3D models of the conduit-like cave to refine the morphometric parameters obtained from the geometric model. These 3D models were then used as input to 3D radar simulations to verify whether they accurately match the observed radar data.

The 3D model of the pit walls, its bottom and the different geometric configurations in its western part were produced by the modelling functions in Blender (v.3.4.1) for the geometry nodes and parametric mesh displace modifiers. The work by Wagner and Robinson[17] on the 3D reconstruction of part of the MTP overhang served to anchor and constrain the 3D model of the cave conduit. The available photogrammetric point cloud of the surface[23] and the MTP[17] were converted into a triangular mesh through a Poisson mesh reconstruction in the software CloudCompare.

As only a few points of the overhang were visible in the point cloud, the vertical pit was modelled based on morphometric parameters in plan view. The depth of the pit was calculated using both the shadow method and the limited information obtained from the point clouds of the photogrammetric reconstruction. This approach was crucial for accurately representing the overhang and the bottom of the pit.

The vertical section of the pit was modelled by filling the gaps in the photogrammetric reconstruction, which had a lower point density than what is required for performing accurate 3D radar simulations after meshing. As a result, the vertical pit was modelled as a cylindrical object with a slightly elliptical plan-view section, using the values from Wagner and Robinson[17] of 100 m and 88 m for the major and minor axes, respectively. The maximum depth of the pit was set to 133 m.

To match the heterogeneity of the cave walls in the photogrammetric model and to reproduce more realistically the radar intensity and the scattering in the 3D simulation output, the simple cylindrical geometry of the pit was deformed through a Blender mesh modifier called the displace modifier. This is typically used to displace the geometry of a smooth object (a cylinder in our case) based on the intensity values derived from a procedurally generated texture (like noise or cloud textures). A cloud texture was exploited as the displacement map to vary the internal geometry of the MTP so that it mimicked the one reconstructed by Wagner and Robinson[17] from LROC imagery. The bottom of the pit was modelled according to the sparse information from the point cloud of Wagner and Robinson[17].

The pile of debris was modelled as a smooth dome with a parametric slope. The bottom of the pit was populated with rocks created with the rock generator procedural function of Blender. The geometry of the rocks was controlled in terms of roundness, skew, size and detail. A set of ten different simple and random rock types were generated with no skew. As shown in Extended Data Fig. 6, boulders were scattered over the pit floor using a random distribution. This was done with the location seed function, which uses a dimensionless value to initialize the random number generator that distributes the geometries on a target surface. We used an initial value that mimicked what could be observed in LROC NAC images. The simulated rocks were generated from a random distribution with diameters between 1 and 4 m. Importantly, neither the type of the size frequency distribution of the rocks nor the density of the rocks per square metre appreciably affected the backscattering response of the 3D radar simulator, which, instead, was affected only by their presence or absence. This is why we used random density, scattering and size distributions that were constrained only by the observable size range.

The cave conduit was modelled in plan view as a cylinder narrowing towards the west. The conduit was generated using a procedurally based cloud modifier, as we did for the vertical pit. The cave-like

conduit inclination, and therefore the slope angle of the pile of debris in section view, were varied in each 3D model from the horizontal to an inclination of up to 70°. The inclinations tested were close to those resulting from the geometric inversion of the radar data. Each 3D model produced was then 3D radar simulated. Within this set of radar simulations, those that best matched the Mini-RF experimental data were selected as the best-fitting models.

3D radar simulations

Simulations were performed with RaySAR[24]. RaySAR is an open-source 3D SAR simulator developed by the German Aerospace Center. RaySAR generates SAR images through a ray-tracing approach using as input a detailed 3D scene input model and the actual acquisition geometry. All the simulated images were computed by assuming the exact same radar parameters and acquisition geometry as the experimental data and by using the available and produced 3D models of the MTP[17].

Selecting the best-fitting model

Let us denote the experimental and the generic simulated Mini-RF amplitude radar images as $A[m,n]$ and $B[m,n]$, respectively. The variables m and n represent the azimuth and range index of the image sample, respectively. The best-fitting model was determined by computing the one-dimensional correlation coefficient between $A[m,n]$ and $B[m,n]$ assuming that m is in the interval $m_0 - 1 \leq m \leq m_0 + 1$ where m_0 is the azimuth coordinate corresponding to the centre of the MTP. The correlation coefficient ρ was computed as:

$$\rho = \frac{1}{3} \sum_{m=m_0-1}^{m_0+1} \frac{\mathrm{cov}(A[m,n],B[m,n])}{\sigma_A \sigma_B}, \quad n_0 \leq n \leq n_1, \quad (8)$$

where cov(.) is the covariance operator and σ_A and σ_B are the standard deviations of $A[m,n]$ and $B[m,n]$ assuming $n_0 \leq n \leq n_1$ and $m_0 - 1 \leq m \leq m_0 + 1$, respectively. The variable n in equation (8) is bounded by the extent of the range response originating from the overhang and conduit defined by the indices n_0 and n_1. The best-fitting model is the one with the highest value of ρ. As a result of the inherent ambiguity in the interpretation of the radar data, two models (denoted as A and B) were selected as being best fitting. This procedure was used to compute the correlation coefficient between the simulated and experimental radar signals displayed in Extended Data Fig. 4. The best-fitting models have an estimation uncertainty for the slope measurement that was also derived from the correlation analysis (Extended Data Fig. 5).

Radar polarimetry and m-chi polarimetric data decomposition

Radar polarimetry exploits the polarization of electromagnetic waves to determine the scattering properties of a target surface. The four Stokes parameters, denoted as S_1, S_2, S_3 and S_4, are defined as:

$$S_1 = \langle |E_\mathrm{H}|^2 + |E_\mathrm{V}|^2 \rangle, \quad (9)$$

$$S_2 = \langle |E_\mathrm{H}|^2 - |E_\mathrm{V}|^2 \rangle, \quad (10)$$

$$S_3 = 2\,\mathrm{Re}\langle E_\mathrm{H} E_\mathrm{V}^* \rangle, \quad (11)$$

$$S_4 = -2\,\mathrm{Im}\langle E_\mathrm{H} E_\mathrm{V}^* \rangle, \quad (12)$$

where E_H and E_V are the horizontal and vertical polarized electric fields composing the radar echoes. S_1 represents the radar echo total power. The degree of polarization m is

$$m = \frac{(S_2^2 + S_3^2 + S_4^2)^{1/2}}{S_1}. \quad (13)$$

The ellipticity χ is related to the degree of polarization and the Stokes parameters in the following way:

$$\sin 2\chi = -\frac{S_4}{mS_1}. \qquad (14)$$

Different types of scattering can be discriminated by defining the following quantities:

$$db = (mS_1(1 + \sin 2\chi)/2)^{1/2}, \qquad (15)$$

$$vs = (S_1(1 - m))^{1/2}, \qquad (16)$$

$$bs = (mS_1(1 - \sin 2\chi)/2)^{1/2}, \qquad (17)$$

where the db parameter is an indicator of double (even) bounce (for example, dihedral) scattering. The vs parameter provides an indication of random polarization (for example, volume scattering). The bs parameter measures the amount of single scattering. These three indicators are combined in an RGB image where db, vs and bs are associated with the red, green and blue channels, respectively.

Radar system specifications and image data format

The SAR images were acquired with the Mini-RF S-band radar system (2.38 GHz, 12.6 cm wavelength) on the LRO satellite at an orbital altitude of about 50 km in monostatic mode. Mini-RF transmits circular polarization and coherently receives orthogonal linear polarizations. We exploited the LRO Mini-RF Map-Projected Calibrated Data Record. The first Stokes parameter image (file name lsz_06587_2s1_eku_10n033) denoted as S1, which represents the total power or total intensity of the received field, and the m-chi polarimetric decomposition the (file names used for generating the decomposition are lsz_06587_2s1_eku_10n033, lsz_06587_2s2_eku_10n033, lsz_06587_2s3_eku_10n033 and lsz_06587_2s4_eku_10n033) were considered in the analyses. The standard look angle range for Mini-RF is from 45°. Given the small size of the imaged pit, the look angle does not appreciably vary across the scene. The image resolution was 15 × 30 m (azimuth × range).

Data availability

The Mini-RF data are available through NASA's Planetary Data System Geoscience Node (https://pds-geosciences.wustl.edu/). Wagner and Robinson's[17] internal morphology point cloud of the MTP is available at https://zenodo.org/records/6622042. The LROC NAC images and DTMs used in this study are publicly available through the Planetary Data System LROC Node at https://wms.lroc.asu.edu/. The data supporting this study are openly available at Zenodo via https://doi.org/10.5281/zenodo.11005458 (ref. 28).

Code availability

All the relevant analyses on the experimental data were performed with MATLAB. RaySAR is open source and available at https://github.com/StefanJAuer/RaySAR.

References

1. Greeley, R. Lava tubes and channels in the lunar Marius Hills. *Moon* **3**, 289–314 (1971).
2. Halliday & William, R. Terrestrial pseudokarst and the lunar topography. *Bull. Natl Speleol. Soc.* **28**, 167–170 (1966).
3. Horz, F. in *Lunar Bases and Space Activities of the 21st Century* (ed. Mendell, W. W.) 405–412 (Lunar and Planetary Institute, 1985).
4. Haruyama, J. et al. Possible lunar lava tube skylight observed by SELENE cameras. *Geophys. Res. Lett.* https://doi.org/10.1029/2009GL040635 (2009).
5. Robinson, M. S. et al. Confirmation of sublunarean voids and thin layering in mare deposits. *Planet. Space Sci.* **69**, 18–27 (2012).
6. Wagner, R. V. & Robinson, M. S. Distribution, formation mechanisms, and significance of lunar pits. *Icarus* **237**, 52–60 (2014).
7. Kaku, T. et al. Detection of intact lava tubes at Marius Hills on the Moon by SELENE (Kaguya) Lunar Radar Sounder. *Geophys. Res. Lett.* **44**, 10–155 (2017).
8. Donini, E., Carrer, L., Gerekos, C., Bruzzone, L. & Bovolo, F. An unsupervised fuzzy system for the automatic detection of candidate lava tubes in radar sounder data. *IEEE Trans. Geosci. Remote Sens.* TGRS.2021.3062753 (2021).
9. Chappaz, L. et al. Evidence of large empty lava tubes on the Moon using GRAIL gravity. *Geophys. Res. Lett.* **44**, 105–112 (2017).
10. Horvath, T., Hayne, P. O. & Paige, D. A. Thermal and illumination environments of lunar pits and caves: models and observations from the Diviner Lunar Radiometer experiment. *Geophys. Res. Lett.* **49**, e2022GL099710 (2022).
11. Kobayashi, T., Kim, J. H., Lee, S. R. & Song, K. Y. Nadir detection of lunar lava tube by Kaguya lunar radar sounder. *IEEE Trans. Geosci. Remote Sens.* **59**, 7395–7418 (2020).
12. Nesnas, I. A. et al. Moon diver: exploring a pit's exposed strata to understand lunar volcanism. *Acta Astronaut.* **211**, 163–176 (2023).
13. Haruyama, J. et al. in *Moon: Prospective Energy and Material Resources* (ed. Badescu, V.) 139–163 (Springer, 2012).
14. Carrer, L., Castelletti, D., Pozzobon, R., Sauro, F. & Bruzzone, L. A novel method for hidden natural caves characterization and accessibility assessment from spaceborne VHR SAR images. *IEEE Trans. Geosci. Remote Sens.* **61**, 1–11 (2022).
15. Nozette, S. et al. The Lunar Reconnaissance Orbiter miniature radio frequency (Mini-RF) technology demonstration. *Space Sci. Rev.* **150**, 285–302 (2010).
16. Raney, R. K. et al. The lunar mini-RF radars: hybrid polarimetric architecture and initial results. *Proc. IEEE* **99**, 808–823 (2010).
17. Wagner, R. V. & Robinson, M. S. Lunar pit morphology: implications for exploration. *J. Geophys. Res.: Planets* **127**, e2022JE007328 (2022).
18. Staid, M. I., Pieters, C. M. & Head, J. W. III Mare Tranquillitatis: basalt emplacement history and relation to lunar samples. *J. Geophys. Res.: Planets* **101**, 23213–23228 (1996).
19. Wagner, R. V. & Robinson, M. S. Occurrence and origin of lunar pits: observations from a new catalog. In *Proc. 52nd Lunar and Planetary Science Conference* (Lunar and Planetary Institute, 2021).
20. Wynne, J. J. et al. Planetary caves: a Solar System view of processes and products. *J. Geophys. Res.: Planets* **127**, e2022JE007303 (2022).
21. Cushing, G. E. Candidate cave entrances on Mars. *J. Cave Karst Stud.* **74**, 33–47 (2012).
22. Sharma, R. & Srivastava, N. Detection and classification of potential caves on the flank of Elysium Mons, Mars. *Res. Astron. Astrophys.* **22**, 065008 (2022).
23. Henriksen, M. R. et al. Extracting accurate and precise topography from LROC narrow angle camera stereo observations. *Icarus* **283**, 122–137 (2017).
24. Auer, S., Hinz, S. & Bamler, R. Ray-tracing simulation techniques for understanding high-resolution SAR images. *IEEE Trans. Geosci. Remote Sens.* **48**, 1445–1456 (2009).
25. Head, J. W. III. Lunar volcanism in space and time. *Rev. Geophys.* **14**, 265–300 (1976).
26. Titus, T. N. et al. A roadmap for planetary caves science and exploration. *Nat. Astron.* **5**, 524–525 (2021).
27. Blank, J. G. et al. *Planetary Caves as Astrobiology Targets*. White Paper (National Academy of Sciences, 2018).

28. Carrer, L. et al. Dataset of 'Radar evidence of an accessible cave conduit on the Moon below the Mare Tranquillitatis pit'. *Zenodo* https://doi.org/10.5281/zenodo.11005458 (2024).

Author contributions

L.C. formulated the concept. L.C., D.C. and L.B. developed the radar theoretical model for explaining the observations. L.C., D.C., R.P. and F.S. designed the experiments. L.C., D.C. and L.B. analysed the radar data. R.P. produced the 3D models of the pit and cave-like conduit. R.P and F.S. provided the geological interpretation of the experimental results. L.B. supervised the research and the related funding project. All authors co-wrote the paper and discussed the results and the related implications.

Competing interests

The authors declare no competing interests.

Additional information

Extended data is available for this paper at https://doi.org/10.1038/s41550-024-02302-y.

Correspondence and requests for materials should be addressed to Leonardo Carrer or Lorenzo Bruzzone.

Peer review information *Nature Astronomy* thanks Chunyu Ding, Tyler Horvath and Matthew Perry for their contribution to the peer review of this work.

Reprints and permissions information is available at www.nature.com/reprints.
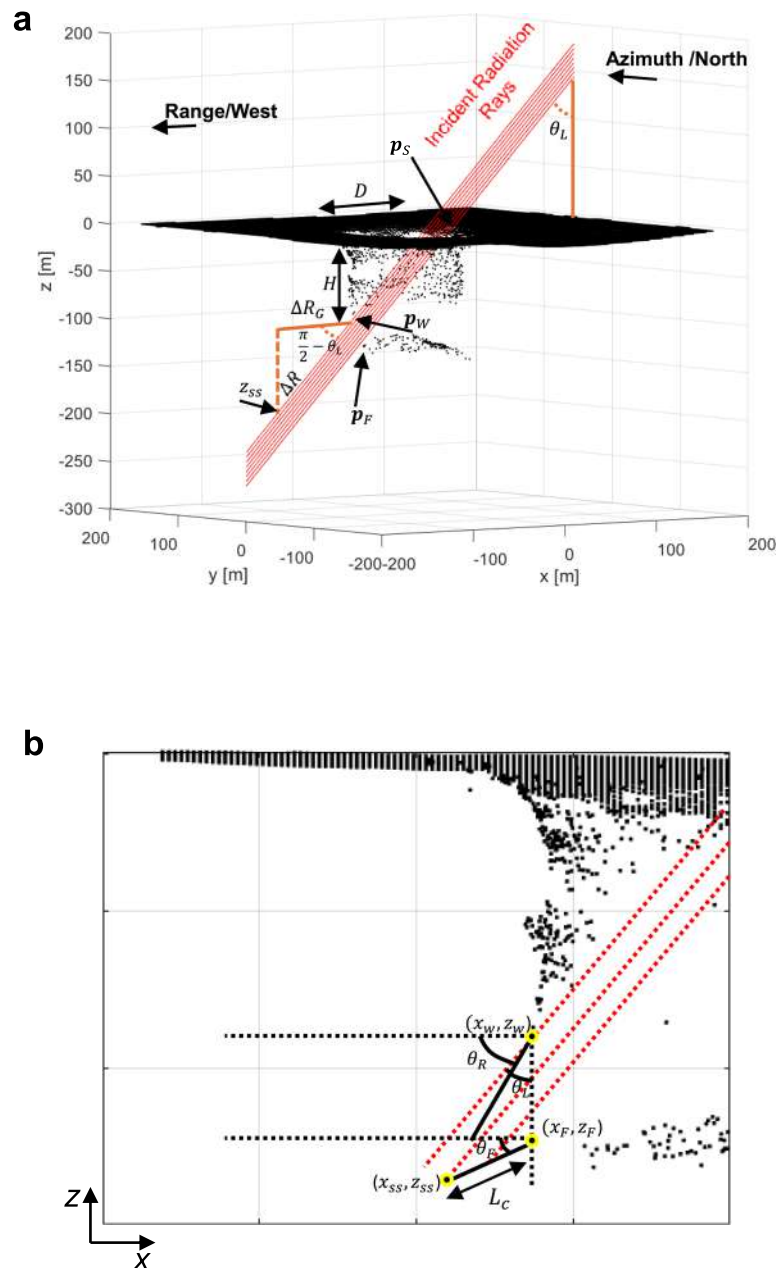
Extended Data Fig. 1 | Wagner and Robinson[17] 3D model of the Mare Tranquillitatis Pit with superimposed geometric quantities. (a) Geometric model with pit characteristics and radar incident rays. The incident radiation rays are depicted for θ_L equal to the one of the Mini-RF acquisition. **(b)** Geometric model detail depicting the parameters involved in the inversion of the cave conduit characteristics. Refer to methods for the description of the variables displayed in the figures.
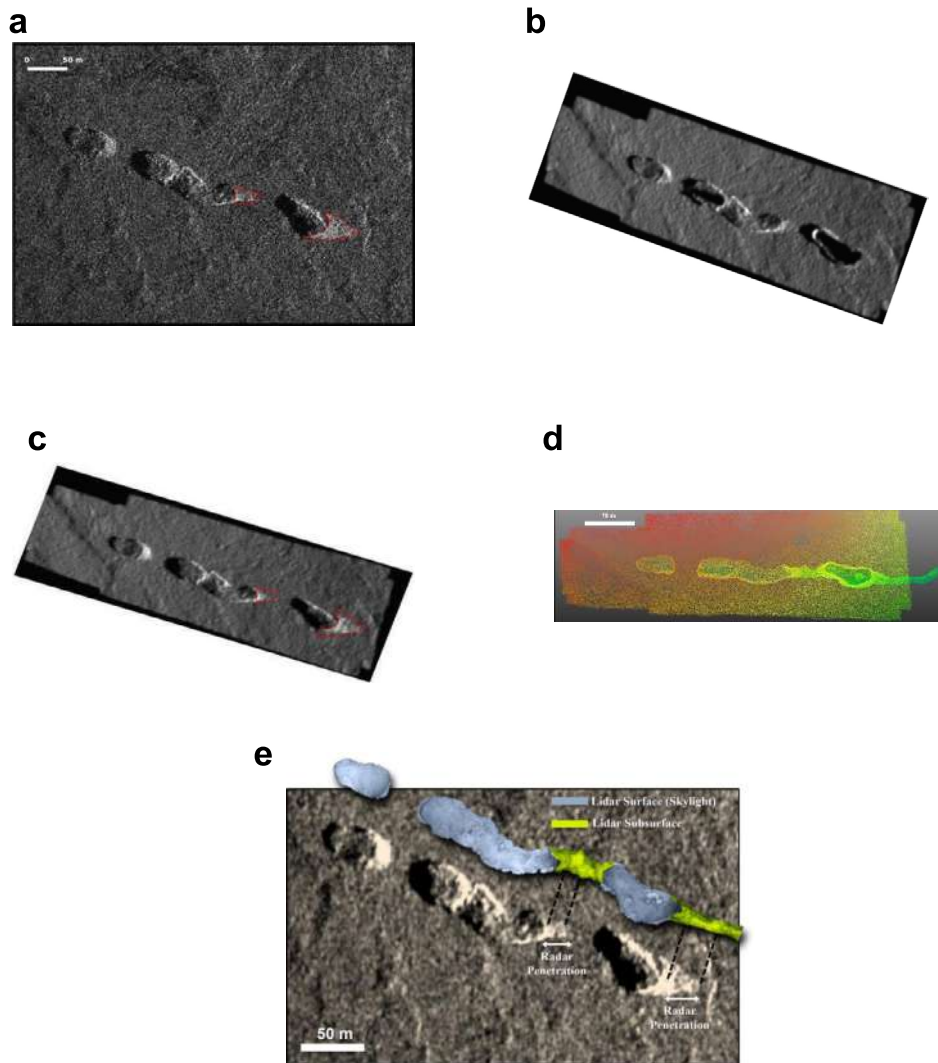
Extended Data Fig. 2 | Comparison between the experimental X-band SAR image and the radar simulation and ground truth of a series of terrestrial analogue pits in Lanzarote, Spain (Lat = 29.165° deg, Lon = −13.454° deg). (a) Capella Space X-band (9.65 GHz) Very High Resolution Synthetic Aperture Radar image[14]. Radar look direction is indicated with a white arrow. (b) 3D radar simulation[24] without subsurface Lidar 3D digital model. (c) 3D radar simulation[24] with subsurface Lidar 3D digital model. The red lines identify the radar response originating from the conduit interior. (d) 3D Lidar scans and drone photogrammetry of the surface (transparency) and the subsurface[14]. Color coding from red to green indicate a progressive increase of the points depth. (e) Superimposition of a detail of the Synthetic Aperture Radar image (Jameo Redondo and Cumplido) with the 3D Lidar scans and drone photogrammetry of the surface and the subsurface[14].
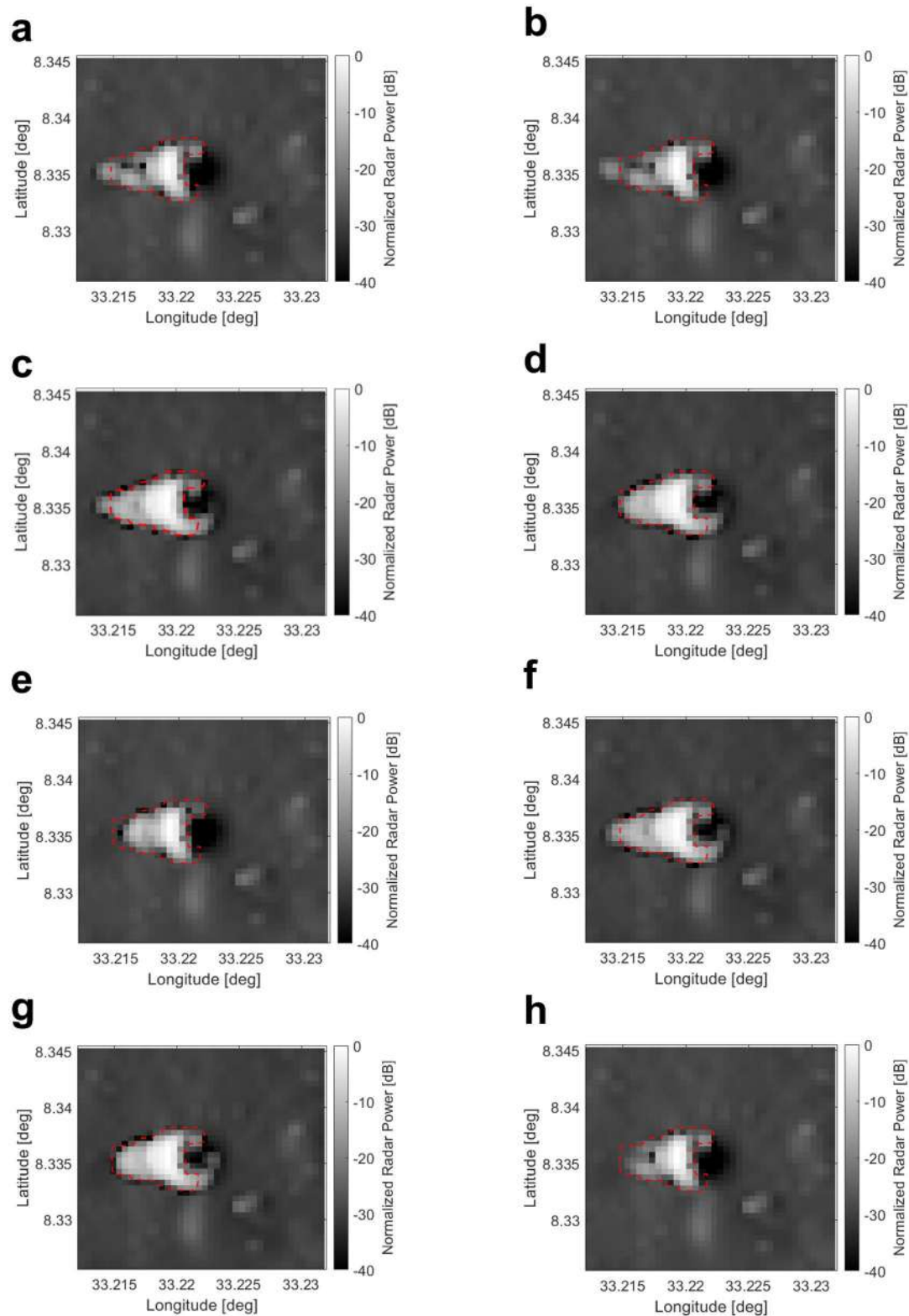
Extended Data Fig. 3 | Additional examples of tested models and 3D Radar Simulations Results. 3D Radar Simulation assuming **(a)** roof and floor slope of 10°, **(b)** roof and floor slope of 20°, **(c)** roof and floor slope of 50°, **(d)** roof and floor slope of 60°, **(e)** roof and floor slope of 80°, **(f)** roof and floor slope of 50° and 40°, **(g)** roof and floor slope of 60° and 40°, **(h)** roof and floor slope of 50° and 60°. The red shape marks the outline of the anomaly in the experimental data (Fig. 1a).
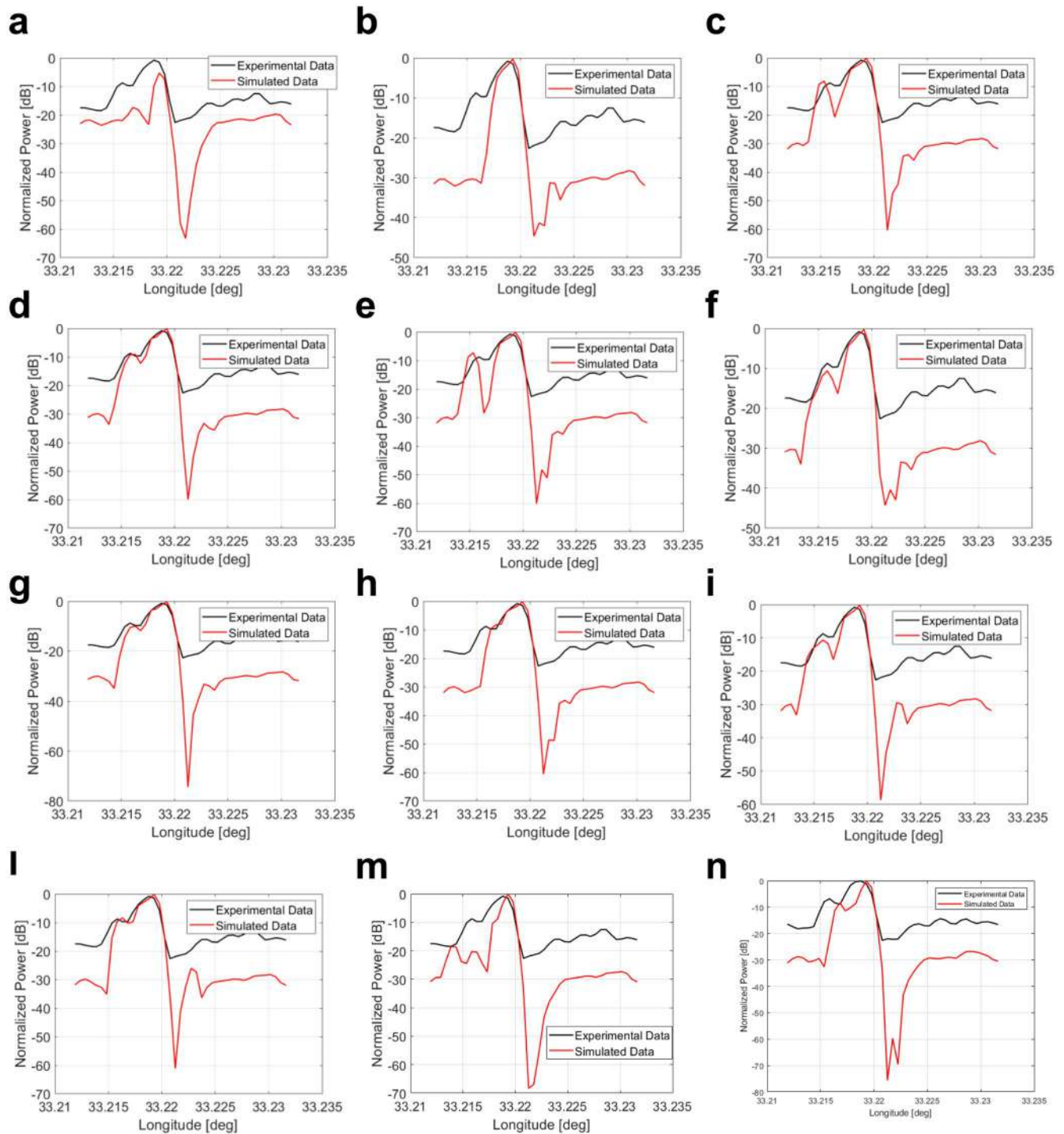
Extended Data Fig. 4 | Examples of the evaluated models latitudinal power profiles. 3D Radar Simulation assuming **(a)** only the surface elevation model, **(b)** Wagner and Robinson's[17] 3D Pit Model (surface and overhang), **(c)** model A (roof and floor slope of 3°), **(d)** model B (roof and floor slope of 55° and 45°), **(e)** conduit roof and floor slope of 5°, **(f)** conduit roof and floor slope of 50°, **(g)** conduit roof and floor slope of 60°, **(h)** conduit roof and floor slope of 70°, **(i)** conduit roof and floor slope of 50° and 40°, **(l)** conduit roof and floor slope of 60° and 40°, **(m)** conduit roof and floor slope of 20° and **(n)** conduit roof and floor slope of 80°. The normalized power profiles are evaluated at a fixed latitude

of about 8.335°. The two power peaks of about 0 dB and -10 dB are the overhang and conduit response, respectively. There is a discrepancy of about 10 dB between the experimental and simulated data in the level of the power response from the lunar surface. This implies that the simulator, as expected, is correctly estimating the scattering contribution from the pit, but underestimating the diffuse scattering contribution from the lunar surface by about 10 dB. However, this does not affect the general validity of the results. The large negative peak of the simulations corresponds to the interior of the pit. This is not shown in the experimental data as due to the Mini-RF dynamic range.

a
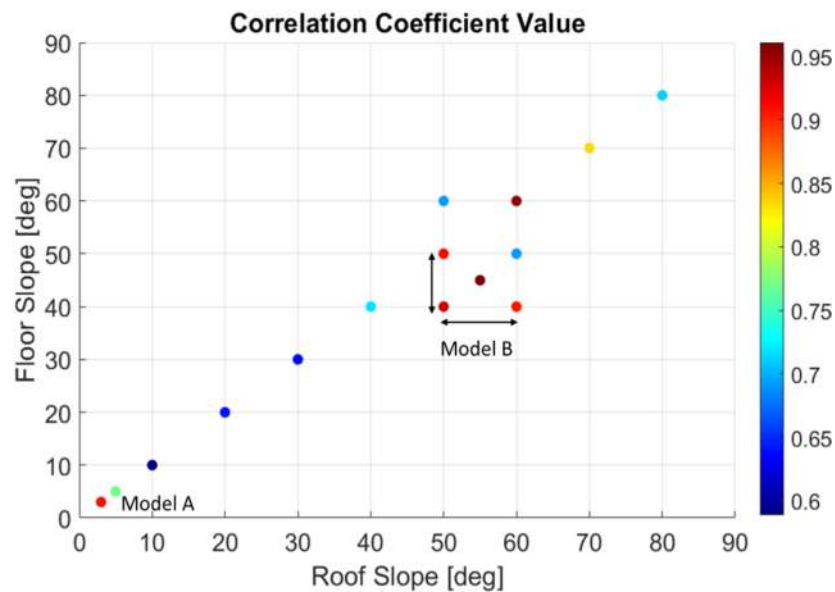
b
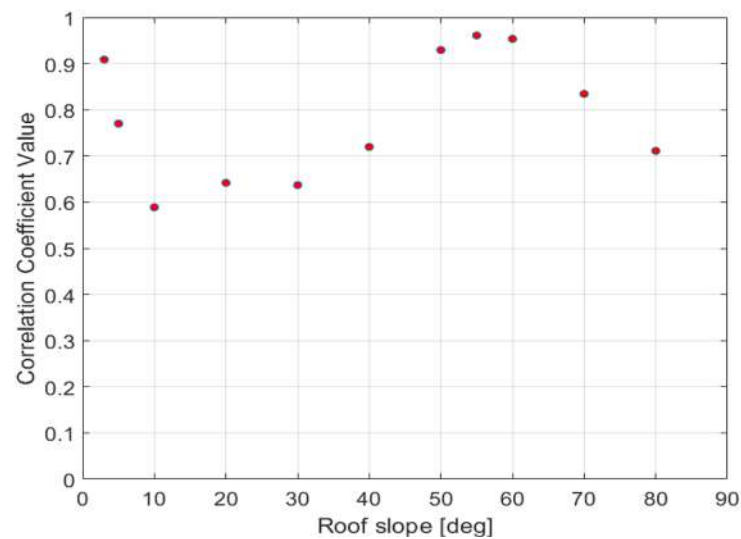
Extended Data Fig. 5 | Results on selection of the best-fitting model through correlation analysis between experimental and simulated radar data.
**(a)** Values of the correlation coefficient (see Methods) between experimental and simulated data versus the roof and floor slopes. The black arrow represents the uncertainty with respect to the best fit model denoted as B. **(b)** Maximum value of the correlation coefficient versus the roof's slope. As a result of the radar ambiguity in determining the cave parameters, the two models denoted as A and B are possible. The range of plausible slopes for which the correlation coefficient yields a high value is in line with what predicted by the radar geometric model for estimating the cave conduit slope from the radar image (see Methods). The correlation coefficient value for the simulated data based on the sole Wagner and Robinson overhang model[17] is equal to 0.66.
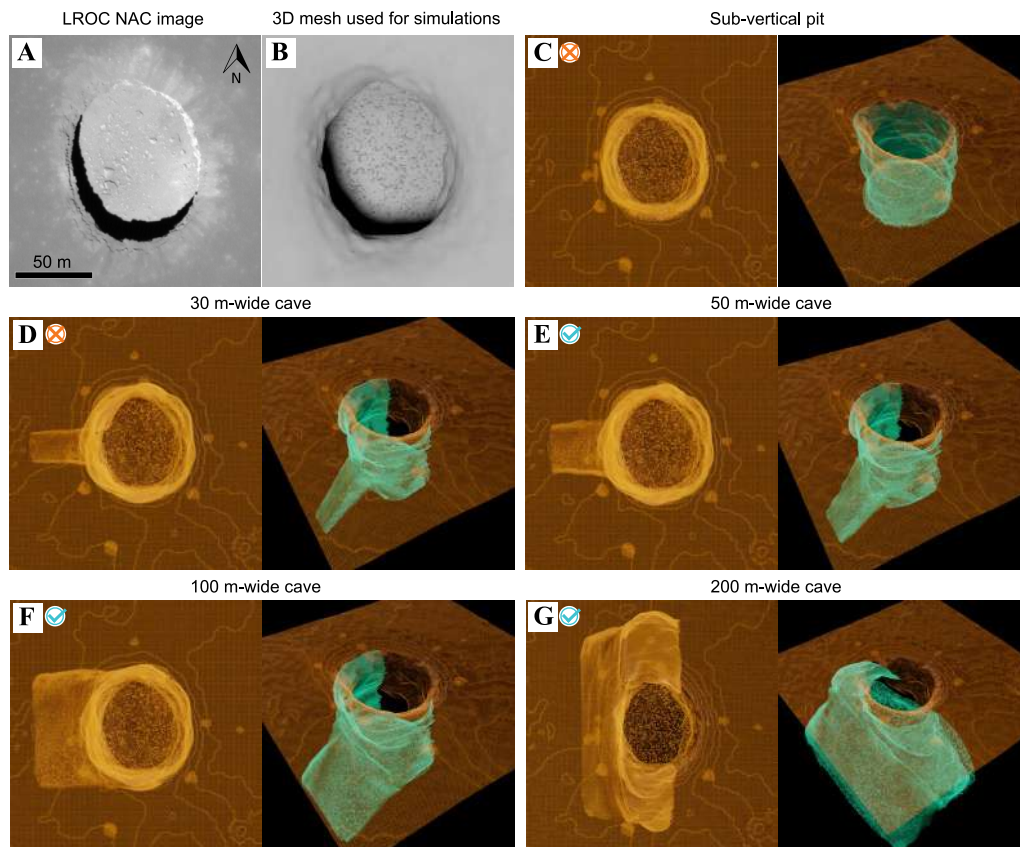
Extended Data Fig. 6 | Comparison between LROC NAC image and the meshed model of the MTP. (a) LROC NAC image M155016845R at 0.41 m/pixel resolution. Notably, two large boulders of 8–10 m of size are located in the south-western side of the MTP's floor. These were not modelled in the procedural rock population generation as they were considered outliers in the global population and also they do not affect the outputs of the simulated Mini-RF response. **(b)** Shaded meshed model of the MTP with the central pit bottom populated by the procedurally generated rocks with geometry nodes with random spatial distribution and a size distribution between 1 m and 4 m. This particular range

of size has been selected based on the boulder's size that can be observed from LROC NAC images of the MTP. **(c, d, e, f, g)** Transparency view of the modelled conduit in plan-view and in perspective view. The LROC NAC DEM and the photogrammetric model by Wagner and Robinson[17] are in orange whereas the procedurally generated pit and cave used for the simulations of the subsurface response to Mini-RF are in cyan. The presence or absence of a cave is simulated, and diameter ranges are displayed here starting from 30, 50, 100 and 200 m. The checkboxes show whether the output of the Mini-RF simulation matches with the observed data or not.
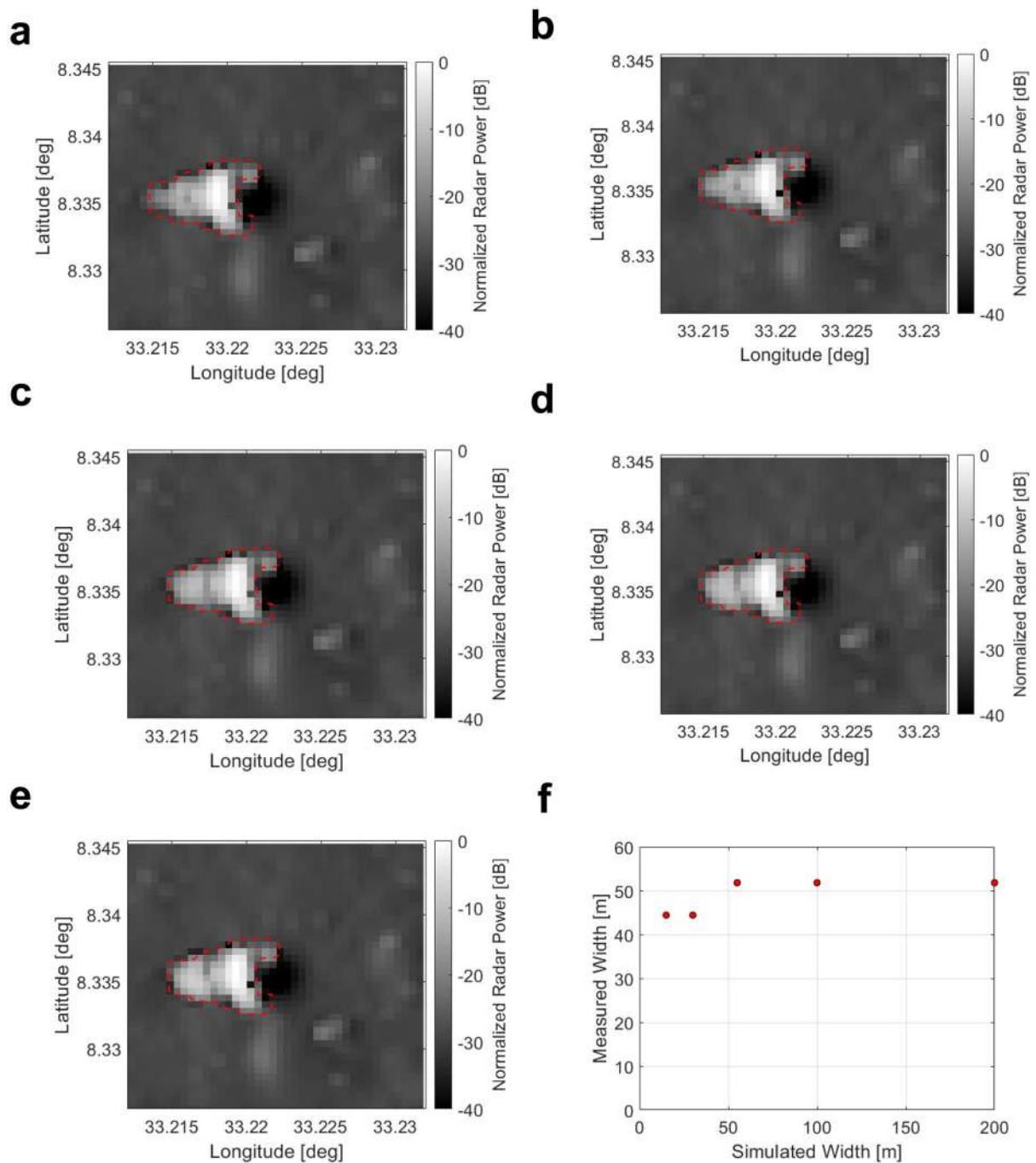
Extended Data Fig. 7 | 3D Radar simulations results for different values of the conduit width. 3D Radar Simulation assuming a conduit width of **(a)** 15 m, **(b)** 30 m, **(c)** 55 m, **(d)** 100 m and **(e)** 200 m. **(f)** Value of the radar measured conduit versus the simulated model cave width. The red shape marks the outline of the anomaly in the experimental data (Fig. 1a).